

Inhomogeneous electronic state near the insulator-to-metal transition in the correlated oxide VO₂

A. Frenzel,¹ M. M. Qazilbash,^{1,*} M. Brehm,² Byung-Gyu Chae,³ Bong-Jun Kim,³ Hyun-Tak Kim,³ A. V. Balatsky,⁴ F. Keilmann,⁵ and D. N. Basov¹

¹*Physics Department, University of California–San Diego, La Jolla, California 92093, USA*

²*Abt. Molekulare Strukturbioologie, Max-Planck-Institut für Biochemie and Center for NanoScience, 82152 Martinsried, München, Germany*

³*IT Convergence and Components Laboratory, Electronics and Telecommunications Research Institute (ETRI), Daejeon 305-350, Korea*

⁴*Theoretical Division and Center for Integrated Nanotechnologies, MS B262, Los Alamos National Laboratory, Los Alamos, New Mexico 87545, USA*

⁵*Max Planck Institute for Quantum Optics–Munich Centre for Advanced Photonics and Center for NanoScience, 85748 Garching, Germany*

(Received 26 May 2009; revised manuscript received 17 July 2009; published 16 September 2009)

We investigate the percolative insulator-to-metal transition (IMT) in films of the correlated material vanadium dioxide (VO₂). Scattering-type scanning near-field infrared microscopy and atomic force microscopy were used to explore the relationship between the nucleation of metallic regions and the topography in insulating VO₂. We demonstrate that the IMT begins within 10 nm from grain boundaries and crevices by using mean curvature and statistical analysis. We also observe coexistence of insulating and metallic domains in a single crystalline grain that points to intrinsic inhomogeneity in VO₂ due to competing electronic phases in the IMT regime.

DOI: 10.1103/PhysRevB.80.115115

PACS number(s): 71.30.+h, 78.67.-n, 78.20.-e, 71.27.+a

I. INTRODUCTION

Correlated oxides of transition metals commonly tend to be heterogeneous on diverse length scales ranging from sub-nanometers to microns.^{1–8} Origins of inhomogeneity in these materials is a subject of ongoing debate. In some materials like high- T_c cuprates,⁹ doping of carriers by dopant atoms was argued to be the source of inhomogeneity. Other correlated materials are stoichiometric, as is the case of vanadium dioxide (VO₂). Yet inhomogeneity is invariably present. It is clear that the detailed microscopic origin of inhomogeneity in correlated systems will depend on the specific properties of the material at hand. Nevertheless, one finds remarkable similarities that possibly point to the same organizing principles of nanoscale phase separation in these materials.

Among the striking common features in correlated oxides is the observation that inhomogeneity is reinforced near phase transitions. Multiple scanning-probe microscopies reveal nanoscale inhomogeneity in the vicinity of phase transitions in correlated materials.^{1–8,10,11} In the vicinity of phase transitions, the system is driven to the point where two different ground states have nearly degenerate free energies and hence any small imbalance including that produced by imperfections will drive the system to different competing states. Even nominally stoichiometric compounds are not free of imperfections. Realistic samples of correlated oxides tend to have dislocations, impurities, oxygen vacancies, twinning, and grain boundaries. It has been hypothesized that such imperfections could serve as nucleation centers for the newborn phase during phase transitions.^{12–16} These defects play the role of pinning centers that stabilize one phase versus another. Hence we would expect that even in materials where inhomogeneity is intrinsic in origin, imperfections will have an important role as pinning centers that reveal

competing states. Experimental evidence for the role of imperfections in phase transitions has been scant primarily because the defects that could serve as nucleation centers have length scales on the order of nanometers or less while there are few nanoscale probes that can be used to simultaneously visualize defects and the seeding of a new phase.

VO₂ exhibits an insulator-to-metal transition (IMT) at $T \approx 340$ K with 4 orders of magnitude change of the dc resistance.^{17,18} In previous work, we employed scattering-type scanning near-field infrared microscopy (s-SNIM) to directly observe the IMT in a polycrystalline film of VO₂.^{8,19} With the aid of s-SNIM, we have demonstrated that the IMT in the bulk of the VO₂ film proceeds via nucleation, growth, and percolation of metallic domains in the insulating host. These metallic domains in the heterogeneous system exhibit enhanced optical mass compared to the macroscopic high-temperature rutile metal.^{8,19} This result indicates that electronic correlations are vital for the occurrence of the IMT and for the presence of the energy gap in insulating VO₂. Further evidence for the importance of electronic correlations is provided by the observation of photoinduced IMT in VO₂.²⁰

In this paper, we present a systematic study of the influence of local topography and the polycrystalline nature of the VO₂ film on the nucleation and growth of metallic domains in insulating VO₂. The s-SNIM technique allows us to investigate infrared contrast produced by electronically dissimilar phases. This technique also allows us to simultaneously obtain topographic images based on atomic-force microscopy (AFM). We acquired detailed and simultaneous infrared and topographic images of the VO₂ film in the IMT regime. Expanding and building on previous work,^{8,19} we obtained optimized topographic images over smaller areas which enabled us to demonstrate the correlation between the film

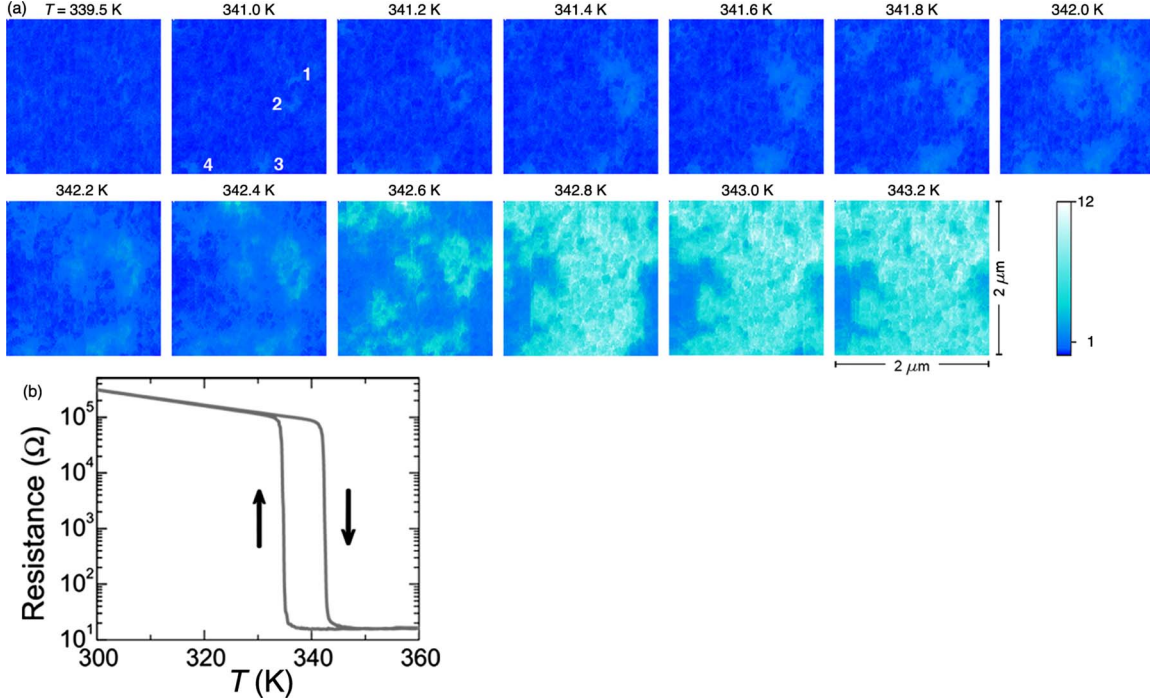


FIG. 1. (Color online) (a) Maps of the second harmonic of the amplitude of the scattering signal collected from the same $2 \times 2 \mu\text{m}^2$ area upon heating the VO_2 film through the IMT. Higher amplitude [light blue (light gray), white] corresponds to the metallic state of VO_2 while lower amplitude [dark blue (dark gray)] corresponds to the insulating state. Four newly formed metallic puddles are marked as 1, 2, 3, and 4 on the $T=341.0$ K map. (b) The temperature dependence of the resistance of the VO_2 film upon heating and cooling through the IMT.

morphology and the nucleation of metallic puddles in the insulating host.

This paper is organized as follows. Sec. II gives a brief overview of sample growth and characterization and describes the basics of the s-SNIM method. Presentation and analysis of data follows this in Sec. III. In Sec. III, we first establish that the topography remains essentially unchanged through the IMT. We then seek to determine where the metallic islands initially nucleate in the sample and whether film morphology influences the location of nucleation sites. We demonstrate that the metallic puddles nucleate primarily near sample defects like grain boundaries. We also show that metallic and insulating regions coexist in single crystalline grains, which is a consequence of competing electronic phases intrinsic to VO_2 . A summary is provided in Sec. IV.

II. SAMPLES AND EXPERIMENTAL METHOD

Highly oriented granular VO_2 films approximately 100 nm thick were grown on $(\bar{1}012)$ oriented sapphire (Al_2O_3) substrates using the sol-gel method. Details of sample growth and characterization are provided in Ref. 21. The resistance of the VO_2 film is plotted in Fig. 1(b) and shows the hysteretic IMT upon heating and cooling. Thin films were used instead of single crystals because the IMT can cause single crystals to fracture.¹⁸ Our thin films have proven to be robust, even after experiencing numerous cycles through the IMT.^{19,22} Thus, data obtained using thin-film samples grown on sapphire substrate are reproducible and can provide information about the intrinsic properties of VO_2 .

The s-SNIM technique uses an AFM in tapping mode to probe the optical properties of materials at the nanoscale while simultaneously acquiring topographic images of the sample surface.²³ The s-SNIM technique relies on polarizing the AFM tip with incident infrared radiation. The extended dipole model, in which the polarized AFM tip is modeled as a spherical dipole, is used to describe the near-field interaction of the tip with the sample.^{19,24} The coupled quasielectrostatic equations of interaction between the tip dipole and the sample can be solved to obtain an effective polarizability of the system, given by

$$\alpha_{\text{eff}}(t) = \frac{\alpha}{1 - \frac{\alpha\beta}{16\pi[a + z(t)]^3}}, \quad (1)$$

where $\alpha = 4\pi a^3(\tilde{\epsilon}_t - 1)/(\tilde{\epsilon}_t + 2)$ is the polarizability of the tip dipole, $\beta = (\tilde{\epsilon}_s - 1)/(\tilde{\epsilon}_s + 1)$ is the response function of the sample, a is the effective radius of the spherical dipole, and $z(t) = z_0[1 + \cos(\Omega t)]$ is the tip-sample distance. Here, Ω is the tapping frequency and z_0 is the amplitude of oscillation. The near-field scattering signal E_s is given by

$$E_s \propto \alpha_{\text{eff}}(1 + r_p)^2 E_i. \quad (2)$$

Here E_i is the incident electric field and r_p is the Fresnel reflection coefficient for p -polarized light. The $(1 + r_p)^2$ factor accounts for the contribution to the near-field signal due to light reflected by the sample.^{19,25,26} Since $\alpha_{\text{eff}}(t)$ depends on the sample's complex dielectric function $\tilde{\epsilon}_s$ and the near-field signal depends on $\alpha_{\text{eff}}(t)$, the model predicts a contrast in

near-field scattering amplitude from materials with different optical properties.²⁷ Further details of the extended dipole model for the specific case of VO₂ are given in Ref. 19.

A home-built AFM with Pt-coated silicon tips was used to map the sample surface and to perform scattering-type scanning near-field infrared microscopy. The VO₂ sample was heated through the IMT, and topographic and near-field infrared images presented in this work were obtained at closely spaced temperature values near the transition temperature. The images were acquired with tapping frequency $\Omega = 25$ kHz and tapping amplitude $z_0 = 40$ nm.²⁴ A CO₂ laser with frequency $\omega = 930$ cm⁻¹ provided the mid-infrared radiation. It is shown elsewhere¹⁹ that there is a significant difference between the optical constants of insulating and metallic phases of VO₂ at this frequency. Thus, the dipole model of the near-field interaction predicts an easily measurable contrast between the scattering amplitude from the metallic and insulating phases at this frequency. We employed a pseudoheterodyne detection scheme with second-harmonic demodulation to extract the genuine near-field scattering amplitude.²⁸ The spatial resolution of s-SNIM is determined by the radius of curvature of the tip and the spatial resolution in our experiment is ≈ 15 nm. The near-field interaction extends to a depth of approximately 20–40 nm into the sample and therefore probes the IMT on length scales on the order of 50 unit cells.²⁹

III. EXPERIMENTAL DATA AND ANALYSIS

Maps of the near-field infrared scattering amplitude spanning the IMT temperature range are shown in Fig. 1(a). The contrast between the scattering amplitude of metallic and insulating phases is evident, in qualitative agreement with the predictions of the dipole model.⁸ High near-field scattering amplitude, which corresponds to the metallic regions of VO₂, is shown as light blue (light gray) and white. Lower scattering amplitude, corresponding to the insulating phase, is indicated by dark blue (dark gray). These images confirm the percolative nature of the IMT, originally reported in Refs. 8 and 19. The optimized topographic images that were acquired simultaneously with the infrared images in the present work, however, reveal new aspects of the IMT that have not been apparent in earlier works reporting the near-field contrast. In order to reveal the correlation between the nucleation of the metallic regions and the thin-film morphology, we acquired the topography and near-field infrared data with greater temperature resolution compared to earlier reports.^{8,19} At $T=296.0$ K, the sample is entirely in the insulating phase and the map shows only small variation in near-field signal, discussed below [Fig. 2(b)]. By $T=341.0$ K, many small regions with increased scattering amplitude appear, signaling the nucleation of metallic puddles. Four of the larger metallic regions are marked on the image acquired at $T=341.0$ K shown in Fig. 1(a). As the IMT progresses, the metallic domains grow and connect until the entire sample is in the metallic phase.

We start the detailed analysis of our topography and near-field images by pointing out that a weak near-field amplitude contrast is present even at room temperature [Fig. 2(b)]. We

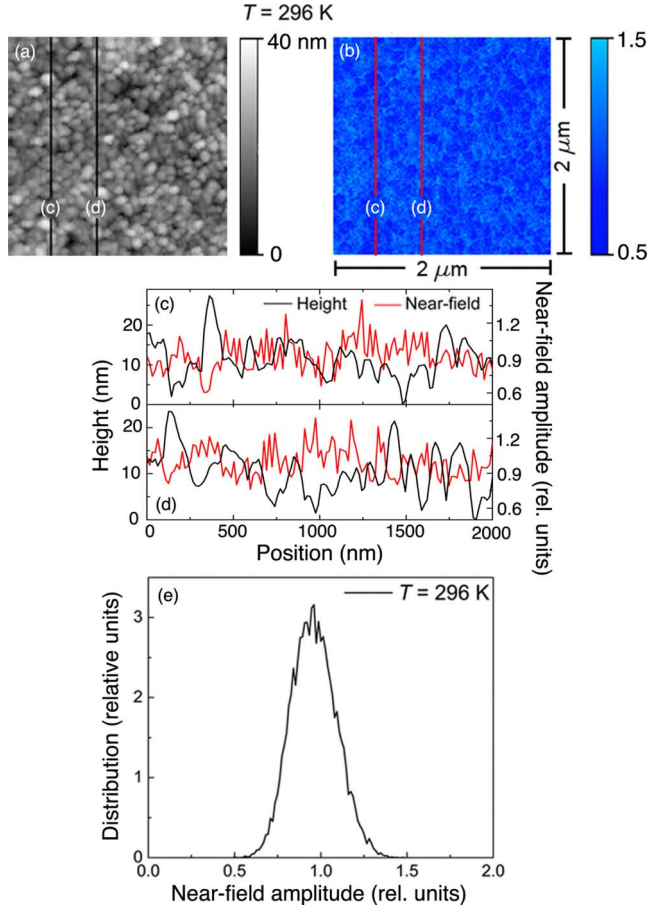


FIG. 2. (Color online) (a) Topography, (b) near-field scattering amplitude (second-harmonic demodulation) map, [(c) and (d)] line profiles taken from top to bottom in (a) and (b), and (e) near-field amplitude distribution at room temperature. The near-field signal is higher where the topography is lower. This is evident in the line cuts [(c) and (d)] that demonstrate the anticorrelation between topography and near-field amplitude. Note that the room-temperature distribution of near-field amplitude (e) is essentially symmetric about the peak, indicating the presence of a single (insulating) phase.

observe that the near-field amplitude signal is slightly higher in topographic valleys and lower on topographic hills by comparing the topography [Fig. 2(a)] to the near-field amplitude [Fig. 2(b)]. The line cuts shown in Figs. 2(c) and 2(d) illustrate this anticorrelated behavior. The contrast present at room temperature is much smaller than that observed at higher temperatures with coexisting insulating and metallic regions. The distribution of the near-field amplitude in Fig. 2(b) is plotted in Fig. 2(e). A single peak with symmetric amplitude distribution at room temperature implies that the entire sample is in the insulating phase. Small variations in near-field signal are likely caused by the sample's local topography and by experimental noise. The dependence of near-field scattering amplitude on mean tip-sample distance predicted by the dipole model in Eq. (1) causes the signal to be slightly higher in topographic valleys and slightly lower on topographic hills for features somewhat larger than the tip size. This is because the average distance between the various points on the convex tip surface and a contacting con-

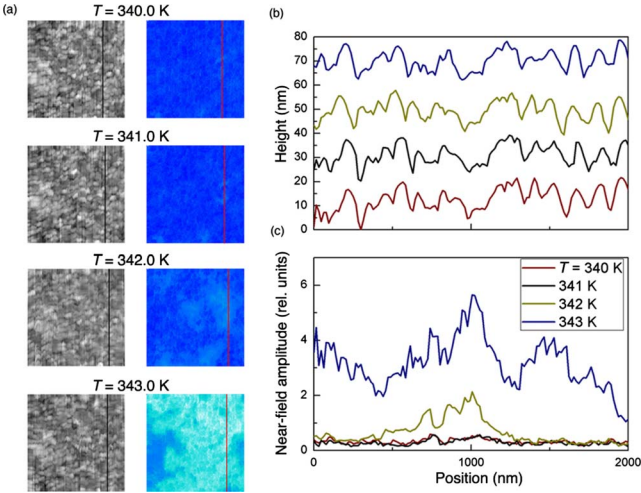


FIG. 3. (Color online) Line profiles taken at the same position in topographic and near-field maps (a) demonstrate that topography remains unaltered while near-field signal greatly increases while heating through the IMT. Drift of the scan area was taken into account to ensure that the profiles were taken at the same location at each temperature. The topographic profiles in (b), offset for clarity, are essentially the same throughout the IMT. The near-field scattering amplitude (c) increases by approximately 1 order of magnitude. Note that the scale for the topographic images is the same as in Fig. 2(a) and the scale for the near-field images is the same as in Fig. 1.

cave sample is smaller than for a contacting convex sample. Since the average grain size is larger than the tip size, we expect this small variation in near-field signal due to topography. Therefore, we propose that the finite width of the distribution in Fig. 2(e) can be partly attributed to topographic variations.

We wish to emphasize that the variations in near-field contrast due to changing optical constants in the IMT regime are substantially larger than the variations due to topographic artifacts. Furthermore, the topography of the films remains unaltered across the transition. Figure 3 shows the line profiles of topographic and near-field amplitude maps (panel a) taken at the same position on the sample at various temperatures. The near-field images are shown on the same scales as those in Fig. 1(a). It is apparent that the topography [Fig. 3(b)] remains essentially constant as temperature increases. In contrast to topography, the near-field signal [Fig. 3(c)] increases significantly. We can therefore conclude that this increase in the near-field signal solely results from the dramatic change in optical constants due to the transition from insulator to metal.

The near-field scattering amplitude distribution at representative temperatures between $T=341$ K and $T=344$ K is displayed in Fig. 4 (solid black line). The distribution that was initially symmetric at room temperature [Fig. 2(e)] acquires an asymmetric tail on the high-amplitude side as the temperature enters the IMT regime (Fig. 4). As the temperature continues to increase, the asymmetry grows and a second peak appears in the distributions of images taken above $T=342.6$ K. Thus, we infer that these tails and peaks correspond to distinct phases of VO_2 . The entire distribution shifts to the high-amplitude values as the IMT nears the end. These

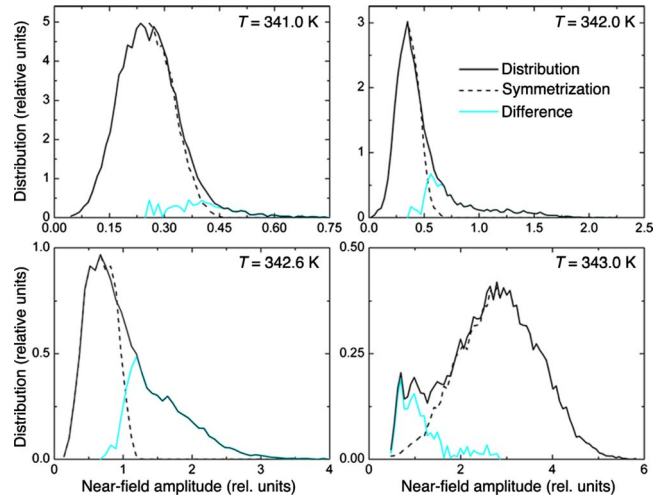


FIG. 4. (Color online) Representative near-field scattering amplitude distributions in the IMT regime, taken from maps shown in Fig. 1. As the temperature approaches the IMT, the raw distribution (solid black lines) develops an asymmetric tail, signifying the beginning of the phase transition. As the temperature increases, the tail grows into a peak, corresponding to the dominance of the metallic phase in the sample. We adopted the following protocol to discriminate between metallic and insulating regions. The dominant peak is symmetrized (dashed lines depict the majority phase) and the difference between the raw distribution and symmetrized peak gives the minority phase [light blue (light gray) lines].

results agree with those obtained using different data, presented in our previous work.^{8,19} The low-amplitude peak in Fig. 4 is centered on the amplitude signal originating from the insulating phase. Likewise, the high-amplitude peak is centered on the scattering amplitude from the metallic regions. The extended dipole model [Eqs. (1) and (2)] predicts the scattering amplitude from metallic regions to be approximately three times the amplitude from the insulating regions. This can be seen in Fig. 4 and is more evident when the histograms in the phase-coexistence regime are normalized to the insulating peak position. A more extensive discussion of the raw and normalized histogram plots is provided in Ref. 19.

Guided by the temperature evolution of the near-field contrast in Fig. 4 we are able to divide the near-field amplitude maps of Fig. 1(a) into insulating and metallic regions. We first assume that the main peak in the amplitude distribution due to the insulating phase remains symmetric at temperatures above room temperature. Thus any asymmetry of distributions with the enhancement of the signal amplitude on the right-hand side of the peak indicates an increase in the contrast due to newly formed metallic regions. This increase in near-field amplitude is two–five times the median amplitude in the insulating phase. The finite distribution of near-field amplitudes from the metallic regions can be attributed to variations in topography and to experimental noise as discussed previously for the insulating phase.

Having assigned the low-amplitude peaks in Fig. 4 to the insulating phase, we symmetrize this portion of the distribution by mirroring the left portion about the well-defined peak. When most of the amplitude distribution has shifted to

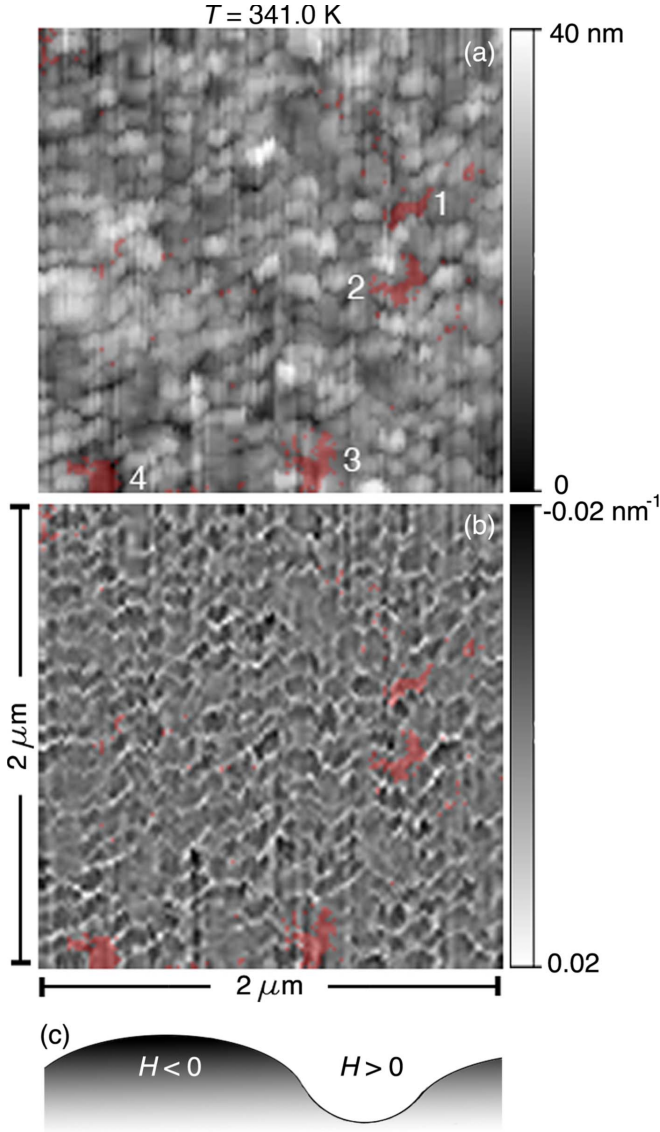


FIG. 5. (Color online) Panel (a) shows high near-field signal overlaid on a $2 \mu\text{m} \times 2 \mu\text{m}$ topographic image taken at $T = 341 \text{ K}$. Metallic regions exhibit high near-field signal and are shown in red. Larger metallic puddles are marked 1, 2, 3, and 4 as in Fig. 1. Panel (b) shows the same near-field amplitude data overlaid on the curvature H of the topography. White corresponds to large positive H , black to large negative H . (c) A sketch showing that the hills in topography correspond to negative H and the valleys correspond to positive H .

the high-amplitude peak at higher temperatures, we symmetrize by mirroring the right portion about the new peak position. By calculating the difference between the actual data (solid black lines) and symmetrized peaks (dashed lines) in Fig. 4, we obtain the contribution of the minority phase [light blue (light gray) lines] to the scattering amplitude. By the minority phase we mean metallic domains at lower temperatures and insulating domains at higher temperatures. By marking points in the near-field amplitude maps originating from the “difference peak,” i.e., those pixels which have scattering amplitude equal to or larger than the value of the peak of the difference curve, we are able to assign locations

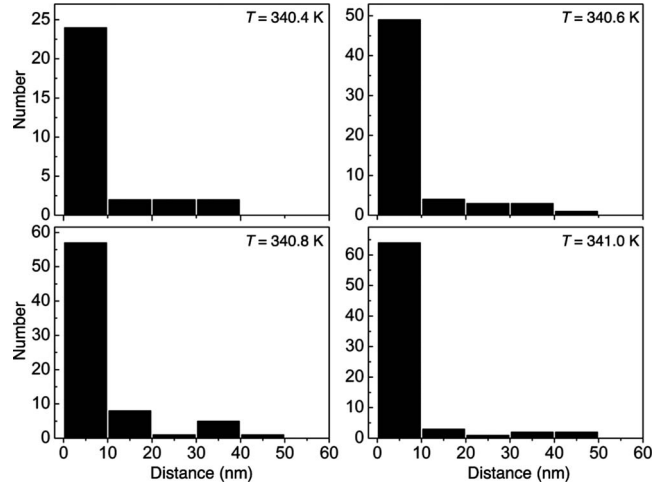


FIG. 6. Histogram displaying the number of metallic puddles with centroid a given distance from grain boundaries.

of the metallic regions near the onset of the IMT.

We overlaid these images of the difference contrast with the topography images in order to compare the two. Figure 5(a) demonstrates the results of the procedure described for the images obtained at $T = 341 \text{ K}$.³⁰ This diagram shows the topographic image with metallic regions marked in red. As in the raw near-field data shown in Fig. 1(a), four main regions (marked as 1–4) of high near-field amplitude are clearly visible by $T = 341.0 \text{ K}$. In addition, a close inspection of Fig. 5(a) reveals that there are many tiny metallic regions lying on grain boundaries. In order to explore the relation between the grain boundaries and the location of metallic puddles more easily, we calculated the curvature H of the topography, using the standard definition

$$H = \frac{1}{2} \frac{\left(1 + \left(\frac{\partial S}{\partial x}\right)^2\right) \frac{\partial^2 S}{\partial y^2} - 2 \frac{\partial S}{\partial x} \frac{\partial S}{\partial y} \frac{\partial^2 S}{\partial x \partial y} + \left(1 + \left(\frac{\partial S}{\partial y}\right)^2\right) \frac{\partial^2 S}{\partial x^2}}{\left(1 + \left(\frac{\partial S}{\partial x}\right)^2 + \left(\frac{\partial S}{\partial y}\right)^2\right)^{3/2}}, \quad (3)$$

where $S = S(x, y)$ is the graph of the surface.³¹ The absolute value of H is largest at points where the direction of the surface normal changes most rapidly, i.e., H is large negative at the peaks of topographic “hills” and large positive at the bottom of topographic “valleys” [see Fig. 5(c)]. We identify the valleys as grain boundaries. A representative image of H , overlaid with the near-field signal from the metallic regions (for $T = 341 \text{ K}$), is displayed in Fig. 5(b). This image reinforces the observation that metallic domains first nucleate around and between grain boundaries. To quantify this observation, we located the centroid of each metallic puddle and measured the distance from the centroid to the nearest grain boundary, which we associate with a maximum in H . We then documented the distributions of these distances. These distributions are displayed as histograms for representative temperatures in Fig. 6. The histograms clearly demonstrate that a vast majority of the newborn puddles are located extremely close to grain boundaries (within $\approx 10 \text{ nm}$). Ad-

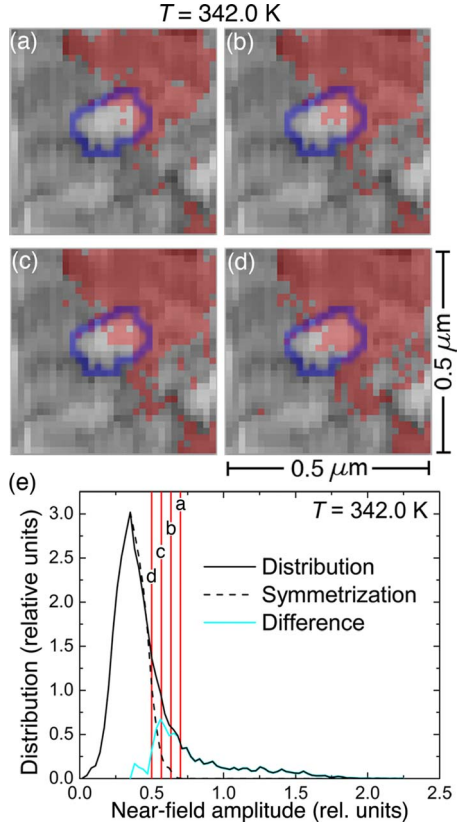


FIG. 7. (Color online) Panels (a) through (d) are topography images overlaid with regions of high near-field infrared signal (metallic regions) in red color. Panels (a) through (d) show a grain that is partly insulating and partly metallic. The grain boundary shown by a thick blue line was determined from the corresponding map of mean curvature H . In these panels, we vary the “cutoff point,” at which we separate the metallic regions (red) from the insulating regions. These images indicate that the observation of phase coexistence in a single grain is not affected by the choice of cutoff point. Panel (e) shows the values of the cutoff points used to create the near-field maps of metallic regions in (a)–(d).

ditionally, the four larger puddles marked in Figs. 1(a) and 5 are either located in grain boundaries or regions of depressed topography. Therefore, we deduce that the IMT nucleates near imperfections such as grain boundaries and crevices. These regions may correspond to sites of increased stress and strain in the film. It is also possible that the electronic properties at the grain boundaries are different from those in the bulk of the grains. Our results therefore suggest that local inhomogeneities in electronic structure and/or strain fields serve as nucleation sites for the metallic instability.³² This observation is in agreement with several previous studies that have detected a change in the critical temperature of the IMT in VO_2 thin films due to effects such as variation in charge-carrier density,^{33,34} stress,^{35,36} strain,^{11,37} and grain size.^{12,15}

Another interesting observation is the occurrence of phase coexistence within single crystalline grains in the VO_2 film. One example of this behavior is shown in Fig. 7. The grain marked in Fig. 7(a) is partly metallic and partly insulating. There is some uncertainty in the precise identification of the

extent of metallic regions in the grain [see Figs. 7(a)–7(d)]. However, it is clear that the grain is partly metallic, independent of the cutoff chosen to identify the metallic regions [see Fig. 7(e)]. Coexistence of metallic and insulating electronic states within a single grain clearly points to phase separation being an intrinsic attribute of the IMT in VO_2 . Thus the role of grain boundaries is to tip the balance locally from the insulating phase to the metallic phase near the IMT when the free energies of these phases are nearly the same.

IV. SUMMARY AND OUTLOOK

Recent advances in diverse scanning-probe techniques have significantly enhanced experimentalists’ abilities to study correlated electron systems at the nanoscale. Our work highlights a unique potential of AFM-based scanning infrared techniques for exploration of correlated electron matter. In this work, we have used simultaneous atomic force microscopy and scattering-type scanning near-field infrared microscopy to investigate the insulator-to-metal transition in VO_2 at the nanoscale level. We show that the IMT is a complex phenomenon, and exhibits nanoscale competition between phases and sensitivity to film morphology. This competition between phases and sensitivity to defects often results in real-space inhomogeneity that is revealed using our s-SNIM technique.

The discussion of inhomogeneity in correlated materials tends to differentiate between the inhomogeneity due to intrinsic effects, such as competing electronic ground states versus extrinsic effects, such as imperfections, defects, and impurities. We explicitly demonstrate that VO_2 is the case that spans both limits. On the one hand by tuning temperature, we drive our material to the point of phase transition where metallic and insulating states are very close in energy, albeit the difference remains finite in case of the first-order transition in VO_2 . One would naturally expect intrinsic inhomogeneity in this correlated material due to spatial variations in the electronic degrees of freedom. On the other hand, even if the inhomogeneity is intrinsic, any extrinsic perturbation will couple to competing order parameters and favor one state or another. Hence near the phase transition, any infinitesimal perturbation will cause local nucleation of competing phases. Therefore, the distinction between extrinsic and intrinsic inhomogeneity is blurred near a phase transition.

We have determined that local topography has an effect on the location of the insulator-to-metal transition’s nucleation sites. We have demonstrated empirically that the metallic islands nucleate at or near grain boundaries and crevices, where variation in electronic properties and strain fields may combine to locally favor the IMT. Despite the fact that defects serve as nucleation sites of the metallic regions, we also find that competing electronic phases are at the heart of inhomogeneity in the IMT regime in VO_2 . This follows from the observation of phase coexistence between insulating and metallic regions in a single crystalline grain. A single crystalline grain is expected to contain few defects and phase coexistence in a grain reveals the true first-order nature of the IMT arising from competing electronic phases.

ACKNOWLEDGMENTS

The authors thank G. O. Andreev for discussions. This work was supported by the U.S. Department of Energy under

Grant No. DE-FG03-00ER45799, the Deutsche Forschungsgemeinschaft Cluster of Excellence Munich-Centre for Advanced Photonics, and the Electronics and Telecommunications Research Institute (ETRI), Korea.

*mumtaz@physics.ucsd.edu

- ¹E. Dagotto, Science **309**, 257 (2005).
- ²V. Emery, S. A. Kivelson, and J. M. Tranquada, Proc. Natl. Acad. Sci. U.S.A. **96**, 8814 (1999).
- ³M. Uehara, S. Mori, C. H. Chen, and S.-W. Cheong, Nature (London) **399**, 560 (1999).
- ⁴L. Zhang, C. Israel, A. Biswas, R. L. Greene, and A. de Lozanne, Science **298**, 805 (2002).
- ⁵J. Lee *et al.*, Nature (London) **442**, 546 (2006).
- ⁶Z. Sun, J. F. Douglas, A. V. Fedorov, Y.-D. Chuang, H. Zheng, J. F. Mitchell, and D. S. Dessau, Nat. Phys. **3**, 248 (2007).
- ⁷K. K. Gomes, A. Pasupathy, A. Pushp, S. Ono, Y. Ando, and A. Yazdani, Nature (London) **447**, 569 (2007).
- ⁸M. M. Qazilbash *et al.*, Science **318**, 1750 (2007).
- ⁹S. A. Kivelson, I. P. Bindloss, E. Fradkin, V. Oganesyan, J. M. Tranquada, A. Kapitulnik, and C. Howald, Rev. Mod. Phys. **75**, 1201 (2003).
- ¹⁰Y. J. Chang, C. H. Koo, J. S. Yang, Y. S. Kim, D. H. Kim, J. S. Lee, T. W. Noh, H.-T. Kim, and B. G. Chae, Thin Solid Films **486**, 46 (2005).
- ¹¹Y. J. Chang, J. S. Yang, Y. S. Kim, D. H. Kim, T. W. Noh, D.-W. Kim, E. Oh, B. Kahng, and J.-S. Chung, Phys. Rev. B **76**, 075118 (2007).
- ¹²D. Brassard, S. Fourmaux, M. Jean-Jacques, J. C. Kieffer, and M. A. E. Khakani, Appl. Phys. Lett. **87**, 051910 (2005).
- ¹³H. K. Kim, H. You, R. P. Chiarello, H. L. M. Chang, T. J. Zhang, and D. J. Lam, Phys. Rev. B **47**, 12900 (1993).
- ¹⁴R. Lopez, T. E. Haynes, L. A. Boatner, L. C. Feldman, and R. F. Haglund, Jr., Phys. Rev. B **65**, 224113 (2002).
- ¹⁵J. Y. Suh, R. Lopez, L. C. Feldman, and R. F. Haglund, Jr., J. Appl. Phys. **96**, 1209 (2004).
- ¹⁶A. V. Balatsky, I. Vekhter, and J.-X. Zhu, Rev. Mod. Phys. **78**, 373 (2006).
- ¹⁷M. Imada, A. Fujimori, and Y. Tokura, Rev. Mod. Phys. **70**, 1039 (1998).
- ¹⁸A. S. Barker, Jr., H. W. Verleur, and H. J. Guggenheim, Phys. Rev. Lett. **17**, 1286 (1966).
- ¹⁹M. M. Qazilbash, M. Brehm, G. O. Andreev, A. Frenzel, P.-C. Ho, B.-G. Chae, B.-J. Kim, S. J. Yun, H.-T. Kim, A. V. Balatsky, O. G. Shpyrko, M. B. Maple, F. Keilmann, and D. N. Basov, Phys. Rev. B **79**, 075107 (2009).
- ²⁰H.-T. Kim, B.-J. Kim, Y. W. Lee, B.-G. Chae, and S. J. Yun, Physica B (Amsterdam) **403**, 1434 (2008).
- ²¹B. G. Chae, H. T. Kim, S. J. Yun, B. J. Kim, Y. W. Lee, D. H. Youn, and K. Y. Kang, Electrochem. Solid-State Lett. **9**, C12 (2006).
- ²²M. M. Qazilbash, A. A. Schafgans, K. S. Burch, S. J. Yun, B. G. Chae, B. J. Kim, H.-T. Kim, and D. N. Basov, Phys. Rev. B **77**, 115121 (2008).
- ²³B. Knoll and F. Keilmann, Nature (London) **399**, 134 (1999).
- ²⁴F. Keilmann and R. Hillenbrand, Philos. Trans. R. Soc. Lond. A **362**, 787 (2004).
- ²⁵A. Cvitkovic, N. Ocelic, and R. Hillenbrand, Opt. Express **15**, 8550 (2007).
- ²⁶M. B. Raschke and C. Lienau, Appl. Phys. Lett. **83**, 5089 (2003).
- ²⁷B. Knoll and F. Keilmann, Appl. Phys. Lett. **77**, 3980 (2000).
- ²⁸N. Ocelic, A. Huber, and R. Hillenbrand, Appl. Phys. Lett. **89**, 101124 (2006).
- ²⁹T. Taubner, F. Keilmann, and R. Hillenbrand, Opt. Express **13**, 8893 (2005).
- ³⁰Tapping-mode operation at elevated temperatures compromises the AFM performance so that the topographic images at higher temperatures (see Figs. 3 and 5) are not as sharp compared to the topographic image obtained at room temperature (see Fig. 2).
- ³¹J. E. Marsden and A. J. Tromba, *Vector Calculus*, 5th ed. (W. H. Freeman and Company, New York, 2003).
- ³²The nucleation of metallic regions occurs near some grain boundaries and in a few low-lying grains. If uneven thermal gradients on the nanoscale were to cause the nucleation of the observed metallic regions then such regions should appear near all grain boundaries and in all grains similarly situated on the substrate as the temperature is increased. We do not observe this and therefore consider it unlikely that nucleation of metallic regions is due to uneven thermal gradients.
- ³³H.-T. Kim, B.-G. Chae, D.-H. Youn, S.-L. Maeng, G. Kim, K.-Y. Kang, and Y.-S. Lim, New J. Phys. **6**, 52 (2004).
- ³⁴B.-J. Kim, Y. W. Lee, B.-G. Chae, S. J. Yun, S.-Y. Oh, and H.-T. Kim, Appl. Phys. Lett. **90**, 023515 (2007).
- ³⁵Y. Muraoka and Z. Hiroi, Appl. Phys. Lett. **80**, 583 (2002).
- ³⁶K. Nagashima, T. Yanagida, H. Tanaka, and T. Kawai, Phys. Rev. B **74**, 172106 (2006).
- ³⁷K. Nagashima, T. Yanagida, H. Tanaka, and T. Kawai, J. Appl. Phys. **100**, 063714 (2006).